Supplementary material for "An Integratible Acoustic Micropump Based on the Resonance of On-Substrate Sharp-Edge Micropillar Arrays"

Yu Zhang,[a] Zeyi Wang,[a], Yang Zhao[a], Qinran Wei[a], Haixiang Zheng[a], Dong Zhang*[ab], and Xiasheng Guo*[ab]

S1. The governing equations for three-dimensional simulations

The models adopted in this study involve the SU-8 micropillar domain (described with the "solid mechanics" interface in COMSOL Multiphysics) and the water domain (the "thermoviscous acoustics" and "laminar flow" interfaces).

In the "solid mechanics" interface, SU-8 is treated as an isotropic elastic material. The mechanical stress tensor σ_1 and the elastic displacement field u_1 in the pillar are coupled with Hooke's Law, which is given by

$$\begin{pmatrix} \sigma_x \\ \sigma_y \\ \sigma_z \\ \sigma_{yz} \\ \sigma_{xz} \\ \sigma_{xy} \end{pmatrix} = \begin{pmatrix} C_{11} & C_{12} & C_{12} & 0 & 0 & 0 \\ C_{12} & C_{11} & C_{12} & 0 & 0 & 0 \\ C_{12} & C_{12} & C_{11} & 0 & 0 & 0 \\ 0 & 0 & 0 & C_{44} & 0 & 0 \\ 0 & 0 & 0 & 0 & C_{44} & 0 \\ 0 & 0 & 0 & 0 & 0 & C_{44} \end{pmatrix} \begin{pmatrix} \partial_x u_x \\ \partial_y u_y \\ \partial_z u_z \\ \partial_z u_y + \partial_y u_z \\ \partial_z u_x + \partial_x u_z \\ \partial_y u_x + \partial_x u_y \end{pmatrix}, \tag{S1}$$

where C_{ij} are the elastic constants. The damping effect in each pillar is introduced through complex-valued elastic coefficients

$$C_{ij} = C'_{ij} + iC''_{ij} = C'_{ij}(1 + i\eta_s), \tag{S2}$$

where $i = \sqrt{-1}$, η_s is an isotropic loss factor. C'_{ij} is determined by Young's modulus E and the Poisson's ratio ν

$$\begin{aligned} C'_{11} &= \frac{E(1-\nu)}{(1+\nu)(1-2\nu)}, \\ C'_{44} &= \frac{E}{(1+\nu)}, \\ C'_{12} &= C'_{11} - 2C'_{44}. \end{aligned} \tag{S3}$$

The Cauchy equation takes the form

$$\nabla \cdot \sigma_1 = -\rho\omega^2 \boldsymbol{u}_1, \tag{S4}$$

where ρ is the material's mass density, $\omega = 2\pi f$ is is the angular frequency, and f is the driving frequency. At the bottom of each micropillar, a velocity boundary ($\boldsymbol{v}_x$) in the x-direction (the side-to-side direction) with a magnitude of 1×10^{-3}m/s is applied by

$$i\omega \boldsymbol{u}_1 = \boldsymbol{v}_x. \tag{S5}$$

In the "thermoviscous acoustics" interface, a perturbation theory is applied to model the system behaviour under harmonic actuation; such a protocol has been previously validated for studying the vibration of sharp edges[1–5]. At this point, the pressure field p and velocity field $\boldsymbol{v}$ can be decomposed into two parts: the 1st-order fields p_1 and $\boldsymbol{v}_1$ that

[a] Key Laboratory of Modern Acoustics (MOE), School of Physics, Collaborative Innovation Centre of Advanced Microstructures, Nanjing University, Nanjing 210093, China. E-mail: guoxs@nju.edu.cn, dzhang@nju.edu.cn
[b] The Collaborative Innovation Center for Cardiovascular Disease Translational Medicine, Nanjing Medical University, Nanjing 211166, China.

oscillates at the angular frequency ω, and the higher-order parts

$$\begin{aligned} p &= p_1 + o(p_1), \\ \boldsymbol{v} &= \boldsymbol{v}_1 + o(\boldsymbol{v}_1). \end{aligned} \tag{S6}$$

For the 1st-order acoustic field, the behaviour of the fluid is described by the Navier-Stokes (NS) equation, the continuity equation and the energy conservation equation, i.e.,

$$\rho_0 \frac{\partial \boldsymbol{v}_1}{\partial t} = -\boldsymbol{\nabla} p_1 + \mu \boldsymbol{\nabla}^2 \boldsymbol{v}_1 + \left(\eta + \frac{1}{3}\mu\right) \boldsymbol{\nabla} (\boldsymbol{\nabla} \cdot \boldsymbol{v}_1), \tag{S7}$$

$$\frac{\partial \rho_1}{\partial t} = -\rho_0 \boldsymbol{\nabla} \cdot \boldsymbol{v}_1, \tag{S8}$$

$$\frac{\partial T_1}{\partial t} = \boldsymbol{\nabla} (D_T \boldsymbol{\nabla} T_1) + \frac{\alpha T_0 \partial \rho_1}{\rho_0 C_p \partial t}. \tag{S9}$$

Here, ρ_0 is the fluid (water) density, η is the bulk viscosity, μ is the dynamic viscosity, ρ_1 is the 1st-order harmonic perturbation of the density, T_1 is the 1st-order harmonic perturbation of the temperature, D_T is the thermal diffusivity, α is the isobaric thermal expansion coefficient, $T_0 = 293.15\text{K}$ is the ambient temperature, C_p is the specific heat capacity at constant pressure. The equation of state is

$$\rho_1 = \frac{p_1}{c_0^2} - \rho_0 \alpha T_1, \tag{S10}$$

where c_0 is the speed of sound.

In the "thermoviscous acoustic-structure boundary" interface, the above two interfaces are coupled with the velocity continuity condition,

$$\boldsymbol{v}_1 = -i\omega \boldsymbol{u}_1. \tag{S11}$$

The "impedance" boundaries are considered as

$$\boldsymbol{n} \cdot \boldsymbol{\nabla} p_1 = -i \frac{\omega \rho_0}{z_i} p_1, \tag{S12}$$

where z_i is the impedance of the corresponding material mimicked at the corresponding boundary.

In the "laminar flow" interface, the wavelength in the fluid (at the centimeter scale) significantly exceeds the dimensions of the sharp edges (at the micrometer scale). Hence, it is appropriate to treat the fluid as incompressible[3], i.e.,

$$\boldsymbol{\nabla} \cdot \boldsymbol{v}_2 = 0, \tag{S13}$$

where $\boldsymbol{v}_2$ is the time-averaged flow velocity. The fluid can be described by the standard NS equation with an additional volume force $\boldsymbol{F}_\text{M}$ arising from the time-averaged acoustic filed[2,3],

$$((\boldsymbol{v}_2 \cdot \boldsymbol{\nabla}) \boldsymbol{v}_2) = \frac{1}{\rho_0} (\boldsymbol{F}_\text{M} - \boldsymbol{\nabla} p_2) + \frac{\mu}{\rho_0} \boldsymbol{\nabla}^2 \boldsymbol{v}_2, \tag{S14}$$

where p_2 is the time-averaged pressure. The volume force is defined as

$$\boldsymbol{F}_\text{M} = -\frac{\rho_0}{2} \text{Re}\left[(\boldsymbol{v}_1 \cdot \boldsymbol{\nabla}) \boldsymbol{v}_1^*\right], \tag{S15}$$

where $\boldsymbol{v}_1^*$ is the complex conjugate of the complex-valued velocity $\boldsymbol{v}_1$.

The channel walls are treated as no-slip boundaries where $\boldsymbol{v}_2 = 0$. The inlet and outlet are set as open boundaries, characterised by a normal stress

$$\mu \boldsymbol{\nabla} \boldsymbol{v}_2 \boldsymbol{n} - p_2 \boldsymbol{n} = -f_0 \boldsymbol{n}, \tag{S16}$$

where f_0 is the normal stress, n is the unit normal vector of the boundary.

S2. The internal flow resistance of the micropump-observation chip system

The pumping pressure is calibrated by measuring the internal flow resistance of the micropump-observation chip system. The flow rate generated by the pressure difference between the inlet and outlet is measured when they are

immersed in two reservoirs positioned at different heights. This measurement is repeated three times for each of the five height differences. The corresponding results are shown in Table S1.

Table S1 Measurement results

Pressure difference (Pa)	Flow rate (nL/s)	Flow resistance (Pa·s/mm^3)
200	42.4	4717.0
	43.1	4640.4
	41.1	4866.2
400	80.7	4956.6
	83.4	4796.2
	81.2	4926.1
600	126.8	4731.9
	127.4	4709.6
	126.1	4758.1
800	169.2	4728.1
	167.1	4787.6
	164.3	4869.1
1000	197.2	5071.0
	208.8	4789.2
	203.2	4921.3

S3. The resonance frequency of an individual micropillar

When the dimensions of the micropillars are overwhelmed by the working wavelength, the vibration behaviour of a micropillar resembles a small rod fixed at one end. The n-th resonance frequency in vacuum, $f_{\mathrm{vac},n}$, is determined as[6],

$$f_{\mathrm{vac},n} = \frac{cK}{2\pi H^2}\kappa_n^2, \tag{S17}$$

where $c = \sqrt{E/\rho}$ is the longitudinal wave speed, with E and ρ being the Young's modulus and the density, respectively. κ_n is an eigenvalue corresponding to the n-th order resonance, which is a constant found elsewhere[6]. For the first-order resonance mode, one has $\kappa_1 = 1.875$. The cross-sectional radius of gyration, K, quantifies the distribution of the cross-sectional area relative to the axis of vibration, it is defined as

$$K^2 = \frac{1}{S}\int r^2 dS, \tag{S18}$$

where r is the distance from a spatial point within the cross-sectional area to the axis; $S = R^2(\pi/2 + \frac{\theta}{2} + 1/\tan\frac{\theta}{2})$ is the surface area of the cross-section. By substituting the geometric parameters of the designed micropillar into Eq. (2), K is obtained as

$$K = 2R\sqrt{\frac{\frac{1}{16}\pi + \frac{1}{16}\theta - \frac{1}{32}\sin(2\theta) + \frac{(\cos\frac{\theta}{2})^2}{3\tan\frac{\theta}{2}} - \frac{(\cos\frac{\theta}{2})^4}{4\tan\frac{\theta}{2}}}{\pi + \theta + \frac{2}{\tan\frac{\theta}{2}}}} = 2R\Theta(\theta). \tag{S19}$$

The first-order resonance frequency in vacuum $f_{\mathrm{vac},1}$ is then

$$f_{\mathrm{vac},1} = 3.5156\frac{cR}{\pi H^2}\Theta(\theta). \tag{S20}$$

As the micropillar is immersed in water, the impact of the surrounding liquid can be described as a correction coefficient[7,8]

$$\frac{f_n}{f_{\mathrm{vac},n}} = \sqrt{\frac{m_\mathrm{s}}{m_\mathrm{s} + m_\mathrm{f}}}, \tag{S21}$$

where f_n is the nth resonance frequency in liquid, $m_\mathrm{s} = \rho S$ is the micropillar's mass per unit height, $m_\mathrm{f} = \rho_0\pi(L\cos\frac{\theta}{2})^2/4$ is the added mass term. Here, ρ_0 is the density of the liquid, and $L = R(1 + 1/\sin\frac{\theta}{2}) + R_0(1 - 1/\sin\frac{\theta}{2})$ is the length of the teardrop cross-section, where R_0 is the round corner's radius at the tip due to actual fabrication.

Finally, the first-order resonance frequency of a micropillar in fluids is determined as

$$f_1 = 3.5156\frac{cR}{\pi H^2}\Theta(\theta)\left\{1+\frac{\pi\rho_0[(1+\frac{R_0}{R})\cos\frac{\theta}{2}+\frac{1-\frac{R_0}{R}]^2}{\tan\frac{\theta}{2}}}{4\rho(\frac{\pi}{2}+\frac{\theta}{2}+\frac{1}{\tan\frac{\theta}{2}})^2}\right\}^{-0.5}. \quad \text{(S22)}$$

S4. Supplementary videos

Video S1: Particle motions recorded in a micropump employing a diamond array of micropillars.

Video S2: The pumping process in the observation chip when the PZT transducer is switched on and off at a frequency of 10 Hz and a duty cycle of 50%.

Video S3: The pumping process in the observation chip when the amplitude of the driving signal is modulated with a sawtooth profile at a modulation frequency of 1 Hz.

Video S4: The pumping process in the observation chip when the amplitude of the driving signal is modulated with a sinusoidal profile at a modulation frequency of 1 Hz.

Video S5: Separation of 10 and 5 μm PS particles recorded in a bright field.

Video S6: Particle motions recorded in a micropump employing a square array of micropillars.

Supplementary Figures

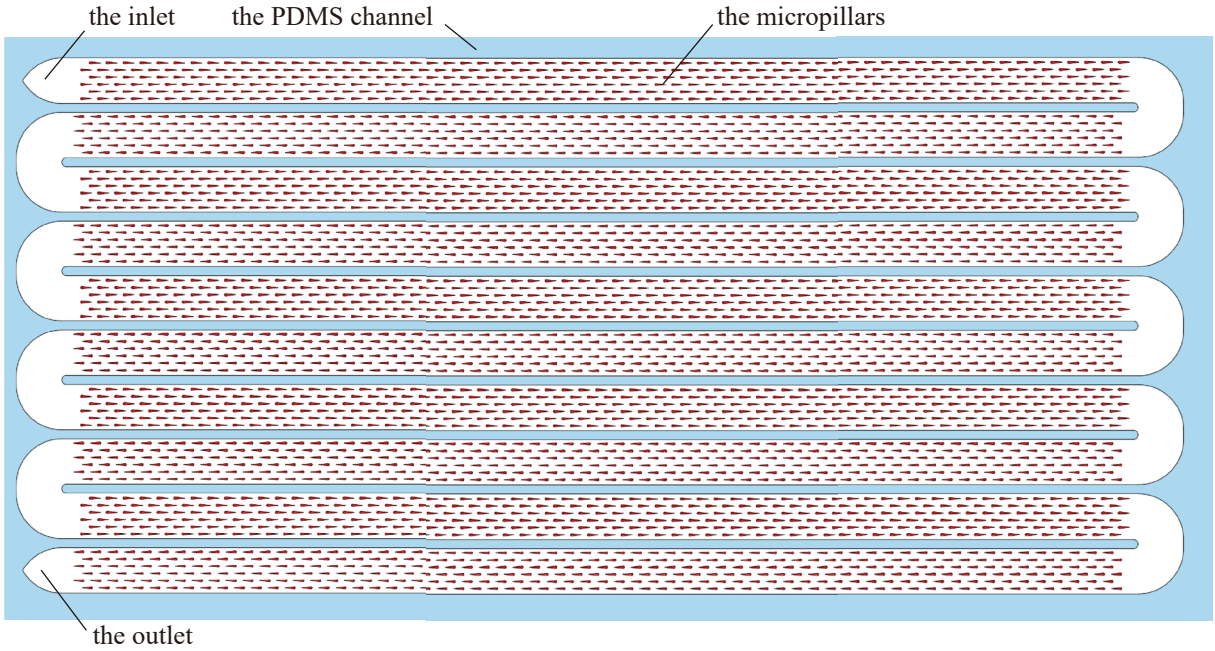

Fig. S1 The design of the micropump (top view).

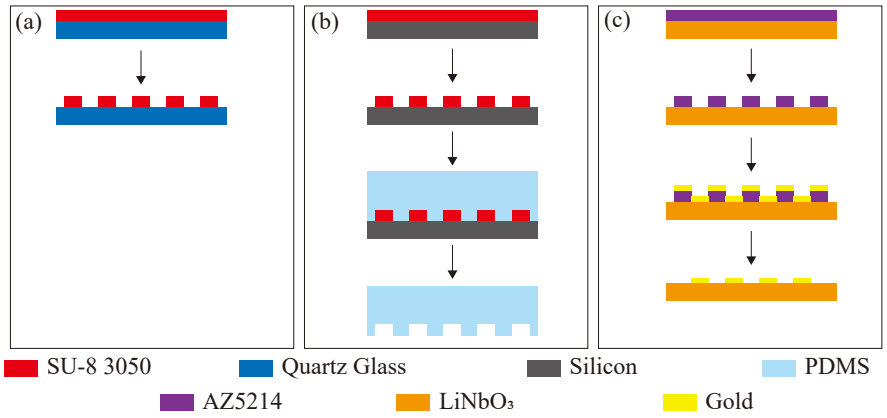

Fig. S2 The fabrication process of the devices. (a) The fabrication of the micropillars includes steps of spin-coating (of SU-8 3050 photoresist) and UV lithography. (b) The fabrication of the microchannel includes steps of spin-coating (of SU-8 3050 photoresist), UV lithography, and PDMS molding. (c) The fabrication of the TaSSAWs device includes steps of spin-coating (of AZ5214 photoresist), UV lithography, magnetron sputtering, and lift-off.

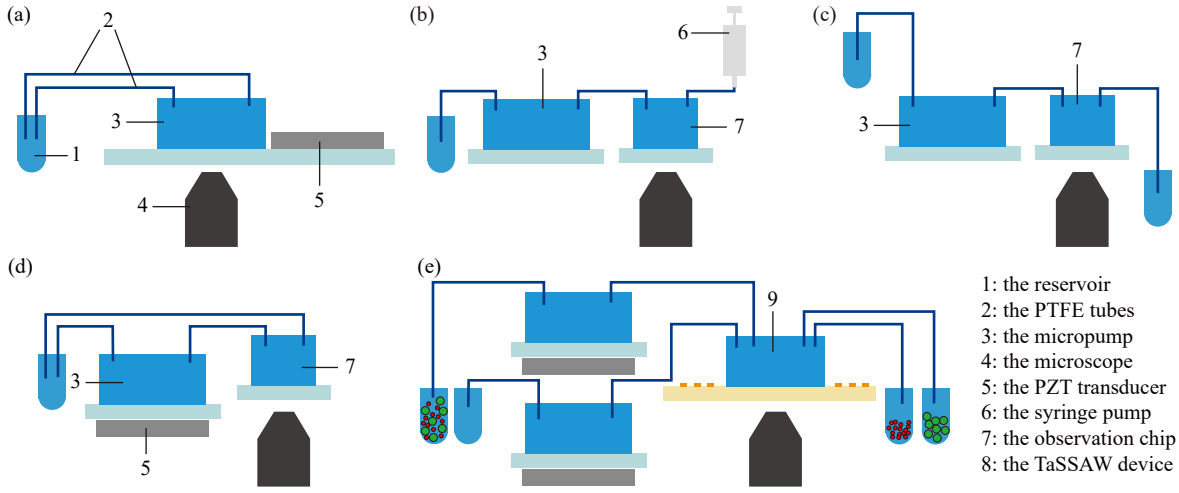

Fig. S3 The experimental setup. (a) PIV measurements to characterise streaming patterns. (b) Calibration of the flow rate. (c) Calibration of the pumping pressure. (d) Characterisation of the micropump performance. (e) Two micropumps are used as feed units for a TaSSAW-based acoustofluidic chip for particle separation.

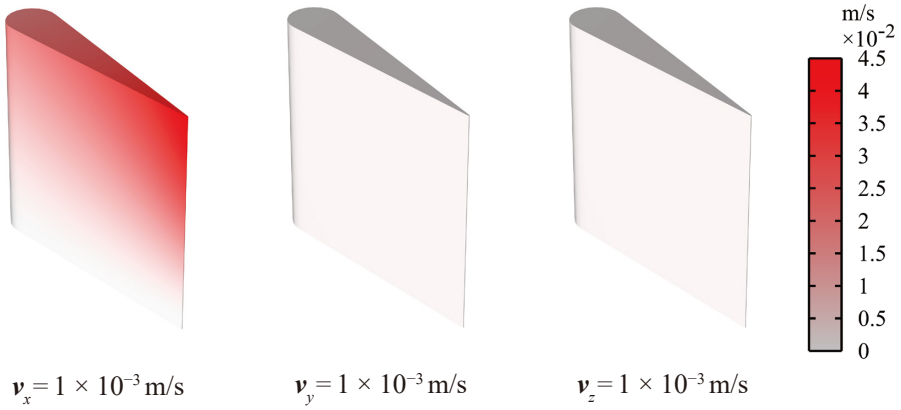

Fig. S4 The velocity distribution of a micropillar actuaged at the bottom in different directions. The results indicate that only the actuation in the x direction can effectively excite the first-order resonance mode.

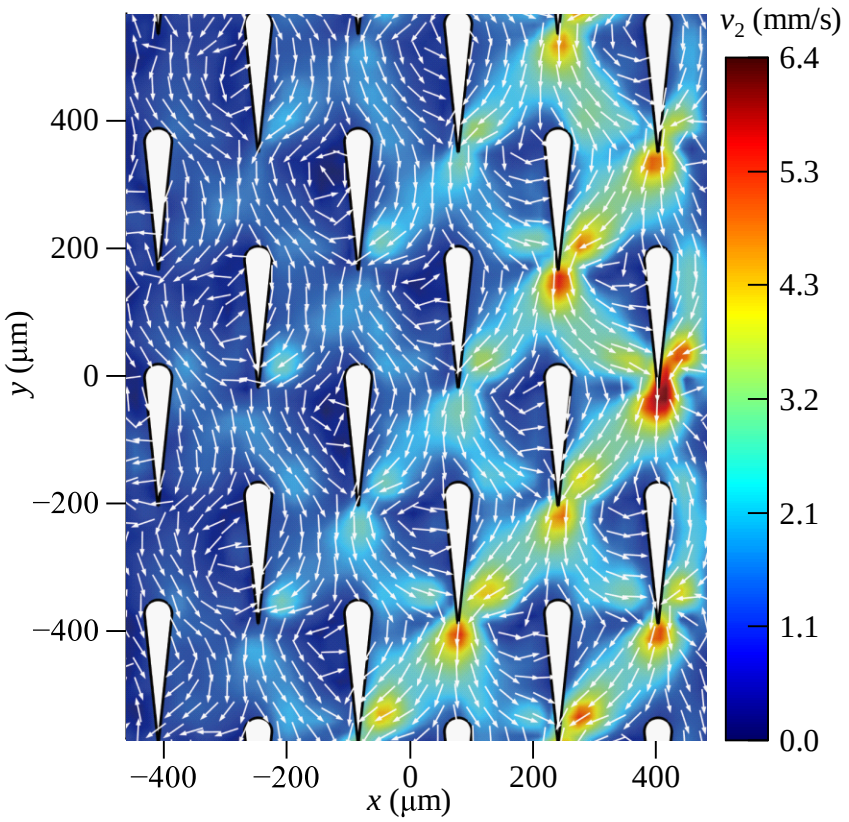

Fig. S5 The tracer velocity map obtained through PIV measurements, corresponding to the streamlines in Fig. 3.

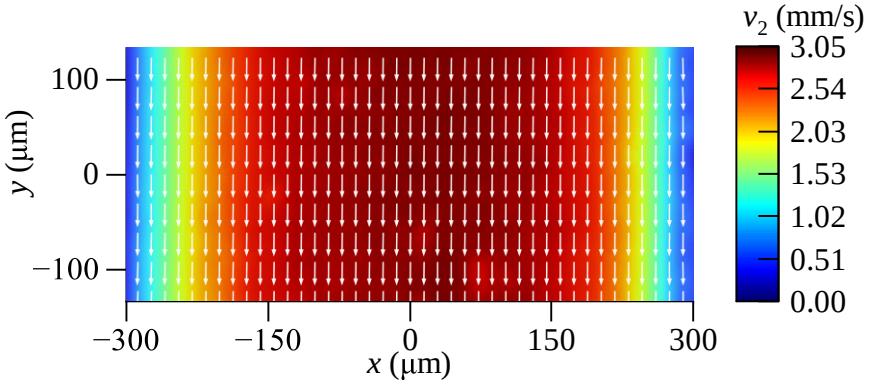

Fig. S6 The tracer velocity map in the observation chip, corresponding to the pumping process driven at a voltage of $V_{\mathrm{p-p}} = 54$ V.

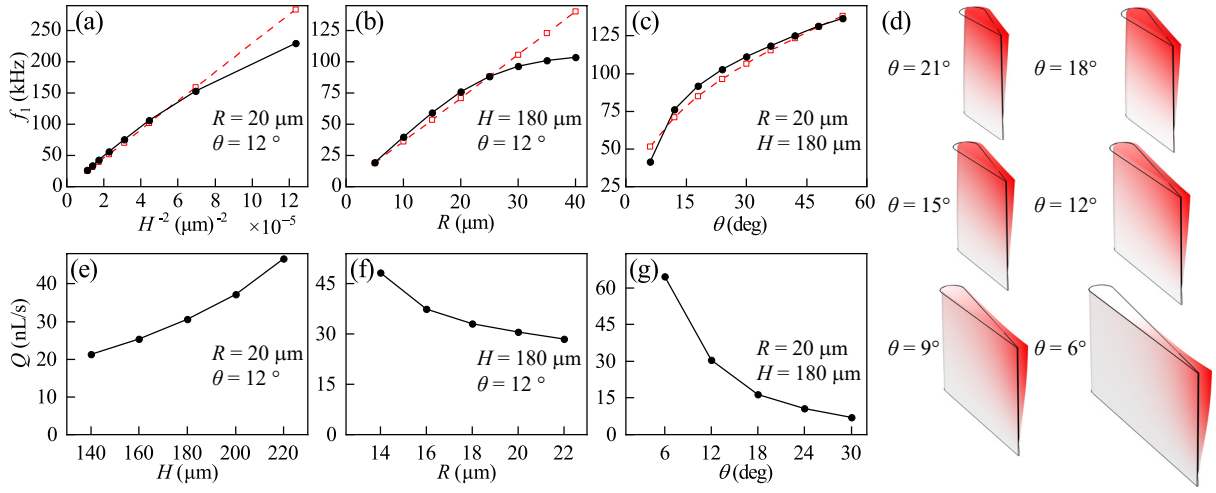

Fig. S7 The performance of a single micropillar. (a)–(c) The dependence of the first-order resonance frequency on the three parameters H, R and θ (black solid lines: FE simulation results; red dashed lines: theoretical predictions). (d) Transition of the resonance mode. (e)–(g) The directional flow rate generated by a single micropillar as H, R or θ varies independently.

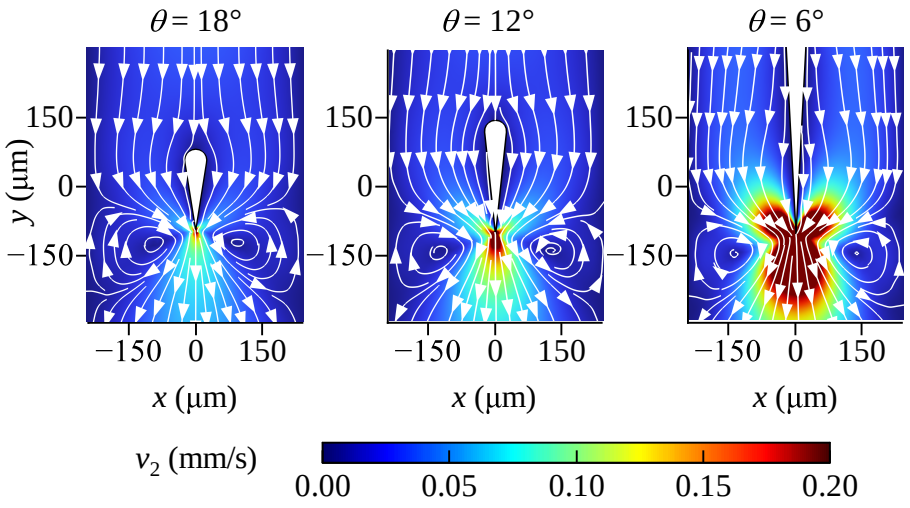

Fig. S8 The streaming pattern generated by a micropillar with different θ.

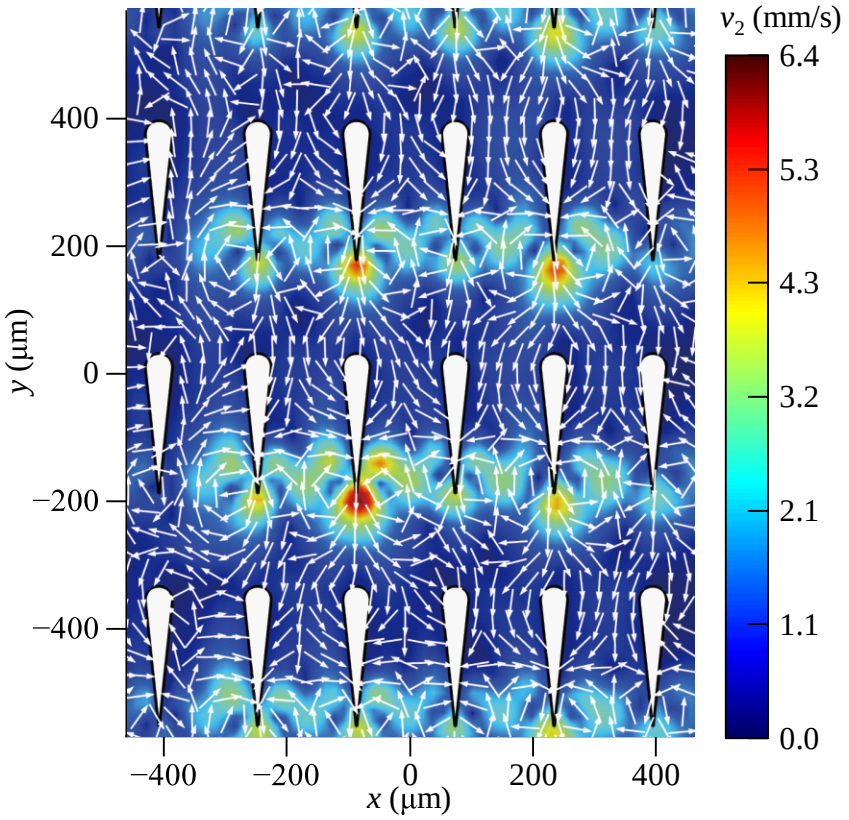

Fig. S9 The tracer velocity field obtained through PIV measurements, corresponding to the streamlines in Fig. 7.

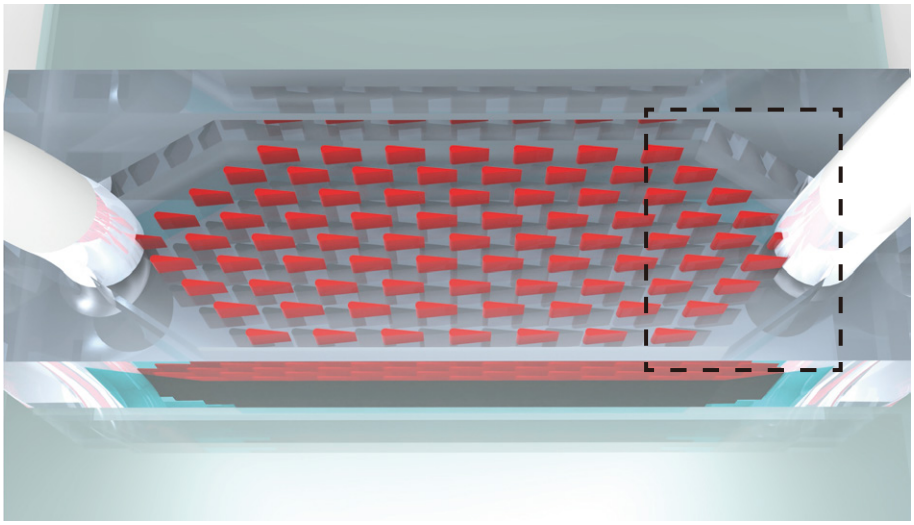

Fig. S10 The schematic diagram of a micropump with a wide channel design. The black square shows the observing region corresponding to Fig. 9.

References

1 A. A. Doinikov, M. S. Gerlt, A. Pavlic and J. Dual, *Microfluid. Nanofluid.*, 2020, **24**, 32.

2 C. Zhang, X. Guo, P. Brunet, M. Costalonga and L. Royon, *Microfluid. Nanofluid.*, 2019, **23**, 104.

3 M. Ovchinnikov, J. Zhou and S. Yalamanchili, *J. Acoust. Soc. Am.*, 2014, **136**, 22–29.

4 N. Nama, P.-H. Huang, T. J. Huang and F. Costanzo, *Lab Chip*, 2014, **14**, 2824–2836.

5 C. Zhang, X. Guo, L. Royon and P. Brunet, *Phys. Rev. E*, 2020, **102**, 043110.

6 P. M. Morse and K. U. Ingard, *Theoretical Acoustics*, Princeton University Press, Princeton, N.J, 1986.

7 M. R. Kramer, Z. Liu and Y. L. Young, *Compos. Struct.*, 2013, **95**, 254–263.

8 M. R. Motley, M. R. Kramer and Y. L. Young, *Compos. Struct.*, 2013, **96**, 365–375.